

Investigating the high-temperature thermoelectric properties of *n*-type rutile TiO₂

S. Thébaud,* Ch. Adessi, and G. Bouzerar

Université Lyon, Université Claude Bernard Lyon 1, CNRS, France



(Received 19 September 2019; published 25 November 2019)

Transition metal oxides are considered promising thermoelectric materials for harvesting high-temperature waste heat due to their chemical and thermal stability, abundance, and low toxicity. Despite their typically strong ionic character, they can exhibit surprisingly high power factors σS^2 , as in *n*-type SrTiO₃ for instance. Thus, it is worth examining other transition metal oxides that might equal or even surpass the performances of strontium titanate. This theoretical paper investigates the thermoelectric properties of *n*-type rutile TiO₂, which is the most stable phase of titanium oxide up to 2000 K. The electronic structure is obtained through density functional theory calculations, while the prominent features of strong electron-phonon interaction and defects states are modeled using a small number of parameters. The thermoelectric transport properties are computed by solving the Boltzmann transport equation with the relaxation time approximation. The theoretical results are compared with a wealth of experimental data from the literature, yielding very good agreements over a wide range of carrier concentrations. This validates the hypothesis of band conduction in rutile TiO₂ and allows the prediction of the high-temperature thermoelectric properties.

DOI: [10.1103/PhysRevB.100.195202](https://doi.org/10.1103/PhysRevB.100.195202)

I. INTRODUCTION

In the past decades, the global energy crisis has led to a renewed interest in the prospect of thermoelectric power generation [1–3]. A great deal of energy is currently wasted as heat in many industrial processes, but could be recovered and put to use if more efficient thermoelectric devices were available, particularly in manufacturing sectors involving high temperatures beyond 1000 K such as metallurgy where furnace temperatures can be as high as 2000 K [4–7]. When it comes to large-scale waste heat recovery, the major stumbling block remains the efficiency of thermoelectric materials. The thermoelectric performance of a given compound is measured by the figure of merit zT :

$$zT = \frac{\sigma S^2}{\kappa} T, \quad (1)$$

where σ is the electrical conductivity, S is the Seebeck coefficient, and κ is the thermal conductivity. κ is usually dominated by the phonon properties, while σS^2 , called the power factor (PF), is governed by electronic transport. The classical materials for high-temperature thermoelectrics, SiGe compounds, exhibit a zT around 1 [8,9]. Widespread industrial use of thermoelectric devices would require an improvement of the figure of merit by a factor 2 to 4 [10,11]. Since the devices are to be placed between a heat source and a heat sink, the ideal thermoelectric material should be stable and efficient over a wide range of temperature.

Recently, transition metal oxides have prompted great interest as potential thermoelectric materials [12–14]. They tend to be stable at high temperatures, composed of earth-abundant elements, and environmentally benign. Although

they are usually strongly polar, they can exhibit surprisingly high power factors. Strontium titanate, in particular, exhibits an excellent room-temperature power factor around $40 \mu\text{W cm}^{-1} \text{K}^{-2}$ [15,16]. However, optimization of bulk SrTiO₃ by doping and nanostructuring has been unable so far to yield figures of merit exceeding 0.5. Therefore, it is worth studying the thermoelectric properties of other transition metal oxides that might equal or even surpass the performances of strontium titanate. Another well-known oxide compound is TiO₂, which comes in three naturally occurring phases: rutile, anatase, and brookite. Of these, rutile is particularly stable at high temperatures with a melting point around 2100 K, while anatase and brookite undergo a phase transition to rutile near 1000 K. Additionally, the carrier concentration of rutile can be tuned by doping with several elements such as boron, niobium, or cobalt, or by using reduction processes to introduce oxygen vacancies acting as electron donors [17–20]. Therefore, this compound would represent a very promising prospect for waste heat recovery applications if its thermoelectric properties could be optimized [21].

In this paper we investigate the electron transport properties of *n*-type rutile TiO₂ by combining first-principle calculations with a modeling of electron-phonon interactions and donor defects. This method allows us to directly compare our results with reported measurements of scattering rates, mobility, electrical conductivity, Seebeck coefficient, and power factor. TiO₂ being a very polar material, it is known that strong interactions between electrons and optical phonons in rutile give rise to the formation of intrinsic small polarons at low temperature, i.e., the electrons are self-trapped by the surrounding deformation of the lattice [22]. This behavior has been observed both experimentally [23] and in density functional theory (DFT) calculations using hybrid functionals [24] or DFT+*U* methodology [25]. On the other hand, the small polarons have been found to be highly unstable

*simon.thebaud@univ-lyon1.fr

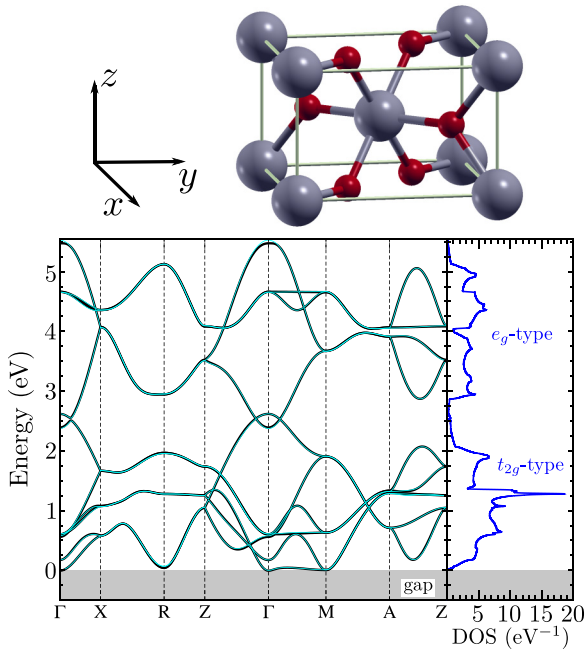


FIG. 1. Top: The conventional cell of rutile TiO_2 , where the gray and red spheres represent the Ti and O atoms, respectively. Bottom: The band structure and density of states of the conduction band, from full DFT calculations (black lines) and from Wannier projections (cyan lines and DOS).

at room temperature and above. Several DFT calculations also find these states to be only slightly favored energetically compared to delocalized conduction states, with an energy barrier hindering the localization of extended electrons [26,27]. Furthermore, the mobility predicted by the small polaron hopping mechanism is orders of magnitude lower than the experimental estimates in reduced samples [28]. The measured mobility above 100 K also decreases when the temperature is elevated [29], suggesting conduction band transport rather than small polaron hopping. Therefore, it is considered likely that the transport properties at room temperature and above are dominated by delocalized electrons (large polarons) in the conduction band. For these reasons, we will investigate the thermoelectric properties of rutile TiO_2 assuming that the electrons are delocalized in the conduction band. Although the standard generalized gradient approximation (GGA) functional of Perdew, Burke, and Ernzerhof (PBE) [30] is unable to describe small polaron states, it predicts the same band structure for the conduction band as the Heyd, Scuseria, and Ernzerhof [31,32] hybrid functional that has been used to investigate small polarons [33]. Therefore, we will compute the conduction band structure with the PBE functional, and we will introduce parameters to model the electron scattering and mass renormalization that are expected to result from strong electron-phonon coupling. These parameters will be set by direct comparison with carrier lifetime and transport measurements.

We perform *ab initio* calculations with the DFT package SIESTA [34] on the rutile structure of TiO_2 (see Fig 1). The GGA-PBE functional and Troullier-Martins norm-conserving pseudopotentials [35] are used. We perform an optimiza-

tion of the double- ζ -polarized basis with the Simplex tool of the SIESTA package. The unit cell is relaxed to forces less than $0.01 \text{ eV}/\text{\AA}$ and to a pressure less than 0.15 kbar. The self-consistent field cycles have been performed with a Monkhorst-Pack of $4 \times 4 \times 4$ k points and a mesh cut-off of 400 Ry. We have checked that the band structure predicted by the plane-wave based DFT package Quantum ESPRESSO [36] is consistent with the results from SIESTA. The electron dispersion and the density of states (DOS) of the conduction band are shown in Fig 1. The black lines corresponds to the SIESTA results, and the cyan lines and the DOS are calculated from Wannier projections of the Bloch states onto the $3d$ orbitals of the Ti atoms, using the Wannier90 software [37]. The ten Wannier orbitals can be classified as low-energy t_{2g} type and high-energy e_g type (more details are given in the Supplemental Material [38]), although even the latter are necessary to accurately describe the bottom of the conduction band. In the Wannier basis, the Hamiltonian matrix elements with an amplitude lower than 1 meV have been cut, which still yields an excellent agreement with the full SIESTA band structure. Since the experimental band gap of rutile TiO_2 is rather large (more than 3 eV), a description of the valence band is unnecessary for the transport properties (we have checked that bipolar conduction is negligible in all our results). The conduction band effective mass in the z direction is $m_b^z = 0.63 m_e$, while the effective masses in the x and y directions are $m_b^x = m_b^y = 1.3 m_e$. There is some anisotropy, but much less than in SrTiO_3 in which the ratio of the effective masses is as high as 10.

II. MODELING ELECTRON TRANSPORT

We calculate the electron transport properties of n -type rutile TiO_2 within the framework of the Boltzmann transport equation (BTE) [39,40], using the relaxation time approximation (RTA). The electrical conductivity and Seebeck coefficients in the i direction ($i = x, y, z$) for a carrier concentration n and a temperature T are given by

$$\sigma_i(n, T) = \int dE \left(-\frac{\partial f}{\partial E} \right) \Sigma_i(E, T) \quad (2)$$

and

$$S_i(n, T) = \frac{-1}{eT\sigma_i} \int dE \left(-\frac{\partial f}{\partial E} \right) (E - \mu_F) \Sigma_i(E, T), \quad (3)$$

where $f(E, \mu_F, T)$ is the Fermi-Dirac distribution and the Fermi level μ_F is determined by integrating the DOS to find the correct electron concentration. $\Sigma_i(E, T)$ is called the transport distribution function (TDF), and its determination is key for the description of electron transport. Solving the BTE with the RTA gives

$$\Sigma_i(E, T) = \frac{2e^2}{\Omega} \sum_{\mathbf{k}, \lambda} v_{\mathbf{k}, \lambda}^i v_{\mathbf{k}, \lambda}^i \tau_{\mathbf{k}, \lambda} \delta(E - \epsilon_{\mathbf{k}, \lambda}), \quad (4)$$

where Ω is the system size, \mathbf{k} runs over the first Brillouin zone, λ is the band index, and the factor 2 accounts for spin degeneracy. $\epsilon_{\mathbf{k}, \lambda}$ is the energy of the eigenstate (\mathbf{k}, λ) , $v_{\mathbf{k}, \lambda}^i = \frac{\partial \epsilon_{\mathbf{k}, \lambda}}{\partial k_i}$ is the velocity in the i direction, and $\tau_{\mathbf{k}, \lambda}$ is the lifetime, considered isotropic for simplicity. The TDF is calculated

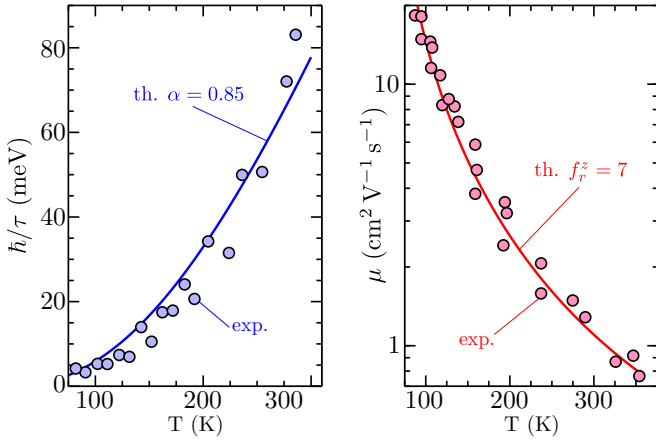


FIG. 2. Left: The experimental (circles, Ref. [43]) and theoretical scattering rate \hbar/τ in meV. The theoretical values correspond to the bottom of the conduction band at the Γ point. Right: The experimental (circles, Ref. [29]) and theoretical mobility μ in the z direction, in $\text{cm}^2 \text{V}^{-1} \text{s}^{-1}$.

using the Drude weight formalism [41,42] (more details are given in the Supplemental Material [38]).

The description of the thermoelectric properties requires an accurate modeling of the electron lifetime. It is especially important to get the correct temperature dependence since we are interested in high-temperature power generation. The scattering rate \hbar/τ has been measured in Ref. [43] from 11 to 300 K. It increases with temperature, exhibiting rather high values around 80 meV at room temperature (see Fig 2, left panel). The temperature dependence between 100 and 300 K is inconsistent with the typical $3/2$ power law of the acoustic deformation potential mechanism, indeed a fit gives an exponent between 2.5 and 3. On the other hand, the large interaction between electrons and optical phonons can be expected to dominate scattering in such a polar compound, provided that the optical modes are sufficiently populated [44]. First-principle calculations [45] and inelastic neutron scattering measurements [46] of the phonon spectrum in rutile TiO_2 indicate the presence of optical modes from 15 to 100 meV. Thus, longitudinal optical (LO) modes should be populated at 300 K and above, leading to a significant polar-optical scattering rate. Assuming a parabolic dispersion for the conduction band electrons and a flat one for the LO branches, second order perturbation theory gives [47,48]

$$\frac{\hbar}{\tau_{\mathbf{k},\lambda}} = \frac{2\alpha}{\sqrt{\epsilon_{\mathbf{k},\lambda}}} \sum_{\nu} (\hbar\omega_{\nu})^{3/2} \left[N_{\nu} \text{Argsh} \left(\sqrt{\frac{\epsilon_{\mathbf{k},\lambda}}{\hbar\omega_{\nu}}} \right) + \Theta(\epsilon_{\mathbf{k},\lambda} - \hbar\omega_{\nu})(N_{\nu} + 1) \text{Argsh} \left(\sqrt{\frac{\epsilon_{\mathbf{k},\lambda}}{\hbar\omega_{\nu}}} - 1 \right) \right], \quad (5)$$

where Θ is the Heaviside function, α is the Fröhlich coupling constant, ν is a branch index running over the LO branches, ω_{ν} is the Γ -point frequency of the branch ν , and $N_{\nu} = 1/(e^{\beta\hbar\omega_{\nu}} - 1)$ is the Bose-Einstein occupation factor. For simplicity, we have included all optical modes in the sum and divided the resulting scattering rate by 3 (a list of

the optical phonon frequencies is given in the Supplemental Material [38]). We have also assumed α to be the same for all modes, thus our scattering law depends only on this single parameter. To set the value of α , we compare the calculated scattering rate at the bottom of the conduction band (see the Supplemental Material [38] for the energy dependence and full temperature dependence of \hbar/τ) with the experimental values between 100 and 300 K. As shown in Fig. 2 (left panel), the choice $\alpha = 0.85$ leads to a good agreement between theory and experiment, thus validating our assumption of dominant polar-optical electron scattering. The temperature dependence of the scattering law (5) (see the Supplemental Material [38]) allows us to describe electron transport at high temperatures beyond 300 K. The value $\alpha = 0.85$ corresponds to a weak Fröhlich interaction with each phonon mode, which is consistent with the use of second order perturbation theory.

Having successfully modeled the temperature-dependent scattering rate, we now endeavor to reproduce the experimental mobilities $\mu = \sigma/ne$ (with n the electron density) that have been measured in Ref. [29] for the z direction. However, if we calculate the TDF from the *abinitio* band structure shown in Fig. 1, the predicted mobility is an order of magnitude higher than the measurements, indicating a large transport mass renormalization of the delocalized carriers due to electron-phonon interactions. This could seem surprising given the relatively low coupling constant $\alpha = 0.85$, but the conduction electrons in rutile TiO_2 interact with five different LO branches: in such cases, the effective coupling constant α_{eff} for a one-branch interaction is given by $\alpha_{\text{eff}} = \sum_{\nu} \alpha_{\nu}$ [49,50]. This gives $\alpha_{\text{eff}} = 4.25$ which corresponds to the intermediate to strong coupling regime, consistent with small polarons that are slightly favored energetically and a large mass renormalization of the delocalized conduction electrons. It is then natural to wonder why the perturbative expression for the scattering rate [Eq. (5)] is validated by experiments, given the strong, nonperturbative value of the overall electron-phonon coupling constant. It must be kept in mind that, for delocalized electrons close to a metal-insulator transition, the single-particle properties (i.e., the band mass and the scattering rate obtained from the spectral function) may not be critical quantities. However, the transport mass associated with the conductivity can be much more sensitive and may be considerably enhanced due to so-called vertex corrections [47]. This scenario resolves the apparent contradiction between a large mass renormalization and the delocalized behavior exhibited by electrons in rutile TiO_2 . To take this effect into account in the simplest way, we introduce the renormalization parameters f_z and $f_x = f_y$ for transport in the z and xy directions, respectively. Only the TDF is renormalized: $\Sigma_i(E, T) \rightarrow \Sigma_i(E, T)/f_i$, and the renormalization parameters are adjusted so that the calculated electronic mobilities reproduce the room-temperature measurements. As shown in Fig. 2 (right panel), the large value $f_z = 7$ leads to an excellent agreement between theory and experiment in the whole temperature range from 100 to 300 K. In the xy direction, the measurements are reproduced by an even larger renormalization factor $f_x = f_y = 23.5$. These values are comparable to the effective masses found in Ref. [29] by fitting the transport measurements.

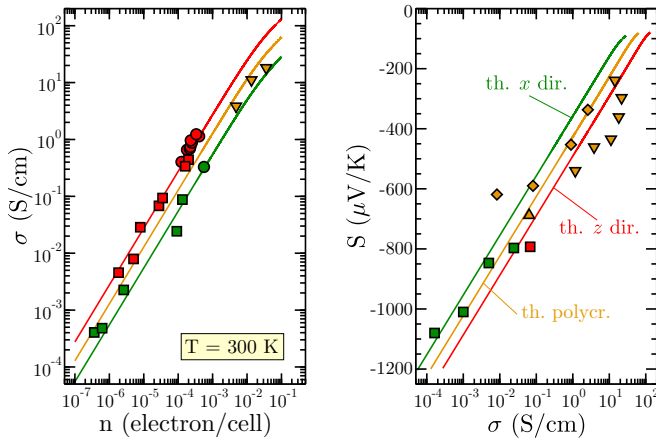


FIG. 3. Left: The predicted room-temperature electrical conductivity in the z direction (red line), the xy directions (green line), and in polycrystalline samples (orange line), as a function of the carrier density n . Right: The predicted Seebeck coefficient as a function of the conductivity for the same directions. The experimental data are taken from Ref. [29] (circles), Refs. [51,52] (squares), Ref. [18] (downward triangles), Ref. [19] (upward triangles), and Ref. [20] (diamonds).

The transport properties can then be calculated as functions of the electron density n , and compared with experimental measurements. We show in Fig. 3 (left panel) the room-temperature electrical conductivity in the z direction (red), in the xy directions (green), and in polycrystalline materials (orange) for which an orientational average was taken. Experimental data from Refs. [18,29,51,52] are also plotted. The agreement between theory and experiment is very good over a wide range of carrier concentration (five orders of magnitude). In the right panel of Fig. 3 is shown the predicted Seebeck coefficient as a function of the conductivity, together with experimental data from Refs. [18–20,51,52]. Although the theory may somewhat underestimate the Seebeck coefficient in some samples, overall it agrees well with experiments.

This success of the theory at 300 K confirms that the electronic transport properties in rutile TiO_2 are consistent with a band conduction mechanism based on delocalized carriers, as opposed to small polaron hopping. Moreover, it should be noted that renormalizing the DOS by the parameters f_z and f_x in addition to the TDF would lead to a large discrepancy between the predicted and measured Seebeck coefficients, due to the Fermi level being pushed further in the gap for a given electron concentration. This supports our hypothesis that the large mass enhancement only applies to the transport mass and that the one-particle properties can be reasonably described by perturbative expressions.

III. HIGH-TEMPERATURE THERMOELECTRIC PERFORMANCES

As high-temperature generation is the main application prospect for TiO_2 as a thermoelectric material, it is crucial to accurately predict the transport properties between 300 and 2000 K. In Ref. [20] the electrical conductivity and Seebeck coefficients of reduced rutile samples, subjected to spark plasma sintering (SPS) at different temperatures, have been measured up to 523 K. The conductivity displays a very weak temperature dependence, even though the scattering rate, Eq. (5), increases substantially with elevated temperature. This suggests an activation mechanism for the electron density in the conduction band, as confirmed by the Hall measurements in Ref. [29] that clearly show an increase of the carrier density with temperature. On the theoretical side, several first-principle calculations of oxygen vacancies in rutile TiO_2 find energetically favored electronic bound states localized on neighboring Ti atoms [24,25,27,53–55]. There is no consensus on the binding energy, although most experimental and theoretical estimates fall between 50 and 200 meV. The situation is similar for Ti interstitials, another important intrinsic defect [56,57], and for extrinsic dopants such as Nb and F substitutions [27].

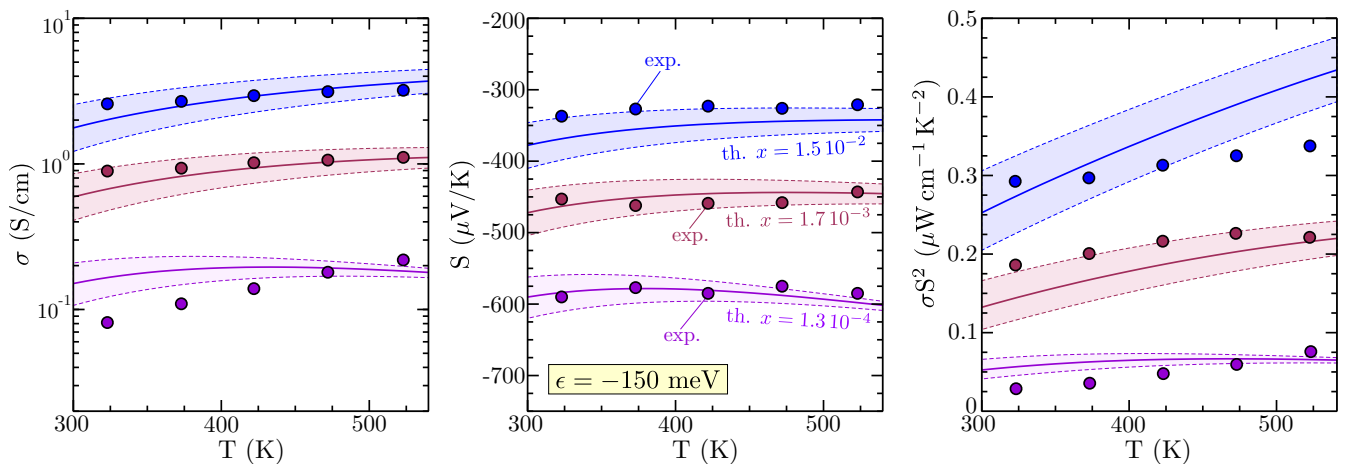


FIG. 4. The predicted electrical conductivity (left), Seebeck coefficient (center), and power factor (right) of polycrystalline TiO_{2-x} as a function of temperature for $x = 1.3 \times 10^{-4}$ (purple), $x = 1.7 \times 10^{-3}$ (red), and $x = 1.3 \times 10^{-2}$ (blue). The shaded regions correspond to a binding energy $\epsilon = -150 \pm 20$ meV. The circles are experimental data from Ref. [20] for three samples subjected to SPS at 1173 (purple), 1273 (red), and 1373 K (blue).

To capture the effects of this activation mechanism in a simple and general way, we model the presence of oxygen vacancies by adding localized defect levels inside the gap at an energy ϵ in the DOS. Thus, TiO_{2-x} is modeled by adding a term $4x\delta(E - \epsilon)$ in the pristine DOS, while the TDF is unchanged (the impurity states have zero conductivity). The total carrier density is set at $4x$ electron/cell (each oxygen vacancy is assumed to bring two electrons), leading to an activation mechanism with more and more carriers populating the conduction band from the defect states as temperature is increased. We adjust the parameters ϵ and x to reproduce the experimental conductivities from the samples in Ref. [20] subjected to SPS at 1173, 1273, and 1373 K. Figure 4 shows the polycrystalline electrical conductivity, Seebeck coefficient, and power factor for $\epsilon = -150$ meV, and three vacancy concentrations $x = 1.3 \times 10^{-4}$, $x = 1.7 \times 10^{-3}$, and $x = 1.3 \times 10^{-2}$. These values lead to a rather good agreement with experimental data, and in particular they reproduce the weak temperature dependence of the conductivities, Seebeck coefficient, and power factor, thus validating our approach. The shaded regions represent the sensibility of the results with respect to ϵ , underscoring that the agreement between theory and experiment is satisfactory given the simplicity of the model (only one temperature and concentration independent impurity level). The important disparities in the predicted vacancy concentration between samples (two order of magnitudes) reflect the measured resistivities that exhibit similarly large variations.

The thermoelectric power factor σS^2 of rutile TiO_2 can now be calculated between 300 and 2000 K. Figure 5 shows the predicted polycrystalline PF as a function of the density n of conduction electrons for several temperatures (top) and as a function of temperature for several oxygen vacancy concentrations (bottom). The optimum carrier concentration is quite large around 0.2 electron/cell, corresponding to a maximum value of $\approx 1.15 \mu\text{W cm}^{-1} \text{K}^{-2}$ (see the inset). Unsurprisingly, a large number of oxygen vacancies (more than 10%) are necessary to provide these carriers, but the activated conduction makes the power factor very stable with temperature between 500 and 1800 K. Still, $1 \mu\text{W cm}^{-1} \text{K}^{-2}$ is a rather low value compared to other oxides such as SrTiO_3 , which has an optimum power factor 40 times larger at room temperature. This poorer performance of titanium oxide is likely caused by two important features of TiO_2 . First, and as noted previously, its band structure exhibits only modest anisotropy due to its crystal structure. In SrTiO_3 , by contrast, the t_{2g} orbitals that make up the conduction bands are oriented along the crystal axis, thus leading to a very two-dimensional character of electron transport. This is not the case in TiO_2 . Second, the electron-phonon interactions lead to a strong mass enhancement and to a lower mobility in TiO_2 than in SrTiO_3 , which is detrimental to the power factor.

The maximum value of the figure of merit zT_{max} in rutile can be roughly estimated assuming an amorphous value $\kappa \approx 1 \text{ W m}^{-1} \text{K}^{-1}$ for the thermal conductivity, as was done in Ref. [21]. This leads to $zT_{\text{max}} \approx 0.15$ around 1800 K. This value is six times lower than the estimate of Ref. [21], which aimed at comparing the different TiO_2 phases and thus did not include the temperature dependence of the scattering rate. Even accounting for the occasional

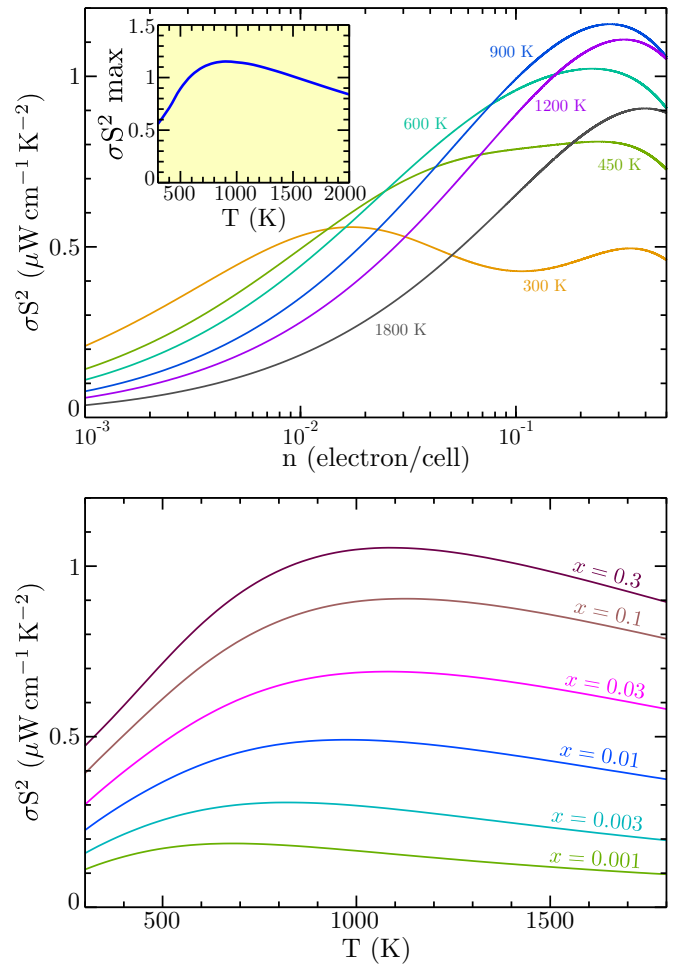


FIG. 5. Top: The polycrystalline power factor σS^2 as a function of the density n of conduction electrons for several temperatures. Inset: The maximum PF as a function of temperature. Bottom: The PF of polycrystalline TiO_{2-x} as a function of temperature for several oxygen vacancy concentrations.

underestimation of the predicted Seebeck coefficient, we do not expect the figure of merit to exceed 0.6, which is insufficient for widespread applications in power generation. Therefore, if rutile TiO_2 is to be useful as a thermoelectric material, significant changes in its electronic structure must be engineered in order to boost the power factor beyond what can be reached by simply increasing the carrier concentration.

IV. SUMMARY AND CONCLUSION

In conclusion, we have investigated thermoelectric transport in n -type rutile TiO_2 through a combination of *ab initio* calculations for the band structure and model descriptions for the electron-phonon interaction and oxygen vacancies. The parameters for the polar-optical coupling scattering rate, mass renormalization, and defect binding energy were set by a comparison between the predicted transport properties and the available experimental measurements. A very good agreement between theory and experiment is obtained over a wide range of carrier concentrations, supporting a band conduction picture of electronic transport

at room temperature and above. We predict a maximum power factor of $1.15 \mu W \text{ cm}^{-1} \text{ K}^{-2}$ reached at 900 K for a large carrier density of 0.2 electron/cell, which requires more than 10% oxygen vacancies in reduced samples. Such a low value of the power factor leads to an estimate of around 0.15 for the maximum figure of merit if the thermal

conductivity is reduced to its amorphous limit. Therefore, the power factor must be boosted significantly before rutile TiO_2 can be widely used as a thermoelectric material in power generation modules. This might possibly be achieved using quantum confinement and energy filtering effects, for instance.

-
- [1] T. Zhu, Y. Liu, C. Fu, J. P. Heremans, J. G. Snyder, and X. Zhao, *Adv. Mater.* **29**, 1605884 (2017).
- [2] X. Zhang and L.-D. Zhao, *J. Materiomics* **1**, 92 (2015).
- [3] X. F. Zheng, C. X. Liu, and Q. Wang, *Renewable Sustainable Energy Rev.* **32**, 486 (2011).
- [4] C. Forman, I. K. Muritala, R. Pardemann, and B. Meyer, *Renewable Sustainable Energy Rev.* **57**, 1568 (2016).
- [5] D. Champier, *Energy Convers. Manage.* **140**, 167 (2017).
- [6] S. LeBlanc, S. K. Yee, M. L. Scullin, C. Dames, and K. E. Goodson, *Renewable Sustainable Energy Rev.* **32**, 313 (2014).
- [7] A. Thekdi and S. U. Nimbalkar, Industrial waste heat recovery - potential applications, available technologies and crosscutting R&D opportunities, Tech. Rep., E3M. Inc North Potomac, Oak Ridge National Lab., TN (2015).
- [8] G. Joshi, H. Lee, Y. Lan, X. Wang, G. Zhu, D. Wang, R. W. Gould, D. C. Cuff, M. Y. Tang, M. S. Dresselhaus *et al.*, *Nano Lett.* **8**, 4670 (2008).
- [9] X. W. Wang, H. Lee, Y. C. Lan, G. H. Zhu, G. Joshi, D. Z. Wang, J. Yang, A. J. Muto, M. Y. Tang, J. Klatsky *et al.*, *Appl. Phys. Lett.* **93**, 193121 (2008).
- [10] L. E. Bell, *Science* **321**, 1457 (2008).
- [11] C. B. Vining, *Nat. Mater.* **8**, 83 (2009).
- [12] Y. Yin, B. Tudu, and A. Tiwari, *Vacuum* **146**, 356 (2017).
- [13] L. Ji, in *Metal Oxides*, edited by Y. B. T. M. O. i. E. T. Wu (Elsevier, Amsterdam, 2018), pp. 49–72.
- [14] H. Ohta, *Mater. Today* **10**, 44 (2007).
- [15] B. Jalan and S. Stemmer, *Appl. Phys. Lett.* **97**, 042106 (2010).
- [16] G. Bouzerar, S. Thébaud, C. Adessi, R. Debord, M. Apreutesei, R. Bachelet, and S. Pailhès, *Europhys. Lett.* **118**, 67004 (2017).
- [17] L. R. Sheppard, T. Bak, and J. Nowotny, *J. Phys. Chem. B* **110**, 22447 (2006).
- [18] H. Kitagawa, T. Kunisada, Y. Yamada, and S. Kubo, *J. Alloys Compd.* **508**, 582 (2010).
- [19] J. Jaćimović, E. Horváth, B. Náfrádi, R. Gaál, N. Nikseresht, H. Berger, L. Forró, and A. Magrez, *APL Mater.* **1**, 032111 (2013).
- [20] Y. Lu, K. Sagara, L. Hao, Z. Ji, and H. Yoshida, *Mater. Trans.* **53**, 1208 (2012).
- [21] D. Bayerl and E. Kioupakis, *Phys. Rev. B* **91**, 165104 (2015).
- [22] J. T. Devreese, Fröhlich Polarons. Lecture Course Including Detailed Theoretical Derivations - 8th edition (2016).
- [23] S. Yang, A. T. Brant, N. C. Giles, and L. E. Halliburton, *Phys. Rev. B* **87**, 125201 (2013).
- [24] P. Deák, B. Aradi, and T. Frauenheim, *Phys. Rev. B* **86**, 195206 (2012).
- [25] L. Zhao, B. Magyari-Köpe, and Y. Nishi, *Phys. Rev. B* **95**, 054104 (2017).
- [26] A. R. Elmaslmane, M. B. Watkins, and K. P. McKenna, *J. Chem. Theory Comput.* **14**, 3740 (2018).
- [27] A. Janotti, C. Franchini, J. B. Varley, G. Kresse, and C. G. Van de Walle, *Phys. Status Solidi RRL* **7**, 199 (2013).
- [28] N. A. Deskins and M. Dupuis, *Phys. Rev. B* **75**, 195212 (2007).
- [29] E. Yagi, R. R. Hasiguti, and M. Aono, *Phys. Rev. B* **54**, 7945 (1996).
- [30] J. P. Perdew, K. Burke, and M. Ernzerhof, *Phys. Rev. Lett.* **77**, 3865 (1996).
- [31] J. Heyd, G. E. Scuseria, and M. Ernzerhof, *J. Chem. Phys.* **118**, 8207 (2003).
- [32] A. V. Krugau, O. A. Vydrov, A. F. Izmaylov, and G. E. Scuseria, *J. Chem. Phys.* **125**, 224106 (2006).
- [33] A. Janotti, J. B. Varley, P. Rinke, N. Umezawa, G. Kresse, and C. G. Van de Walle, *Phys. Rev. B* **81**, 085212 (2010).
- [34] J. M. Soler, E. Artacho, J. D. Gale, A. García, J. Junquera, P. Ordejón, and D. Sánchez-Portal, *J. Phys.: Condens. Matter* **14**, 2745 (2002).
- [35] N. Troullier and J. L. Martins, *Phys. Rev. B* **43**, 1993 (1991).
- [36] P. Giannozzi, S. Baroni, N. Bonini, M. Calandra, R. Car, C. Cavazzoni, D. Ceresoli, G. L. Chiarotti, M. Cococcioni, I. Dabo *et al.*, *J. Phys.: Condens. Matter* **21**, 395502 (2009).
- [37] A. A. Mostofi, J. R. Yates, Y.-S. Lee, I. Souza, D. Vanderbilt, and N. Marzari, *Comput. Phys. Commun.* **178**, 685 (2008).
- [38] See the Supplemental Material at <http://link.aps.org/supplemental/10.1103/PhysRevB.100.195202> for details about the Wannier orbitals, the practical computation of the transport properties, and the calculated electron-phonon scattering rate.
- [39] N. W. Ashcroft and N. D. Mermin, *Solid State Physics* (Saunders College, Philadelphia, PA, 1976).
- [40] M. S. Dresselhaus, *Solid State Physics, Part I: Transport Properties of Solids* (2001).
- [41] W. Kohn, *Phys. Rev.* **133**, A171 (1964).
- [42] D. J. Scalapino, S. R. White, and S. Zhang, *Phys. Rev. B* **47**, 7995 (1993).
- [43] M. Bonn, F. Wang, J. Shan, T. F. Heinz, and E. Hendry, in *Femtochemistry and Femtobiology*, edited by M. M. Martin, J. T. B. T. F. Hynes, and Femtobiology (Elsevier, Amsterdam, 2004), pp. 517–520.
- [44] J. Sjakste, N. Vast, M. Calandra, and F. Mauri, *Phys. Rev. B* **92**, 054307 (2015).
- [45] I. Lukačević, S. K. Gupta, P. K. Jha, and D. Kirin, *Mater. Chem. Phys.* **137**, 282 (2012).
- [46] J. G. Traylor, H. G. Smith, R. M. Nicklow, and M. K. Wilkinson, *Phys. Rev. B* **3**, 3457 (1971).
- [47] G. D. Mahan, *Many Particle Physics, Third Edition* (Plenum, New York, 2000).
- [48] M. Lundstrom, *Fundamentals of Carrier Transport*, 2nd ed. (Cambridge University Press, Cambridge, 2000).
- [49] J. T. Devreese, S. N. Klimin, J. L. M. van Mechelen, and D. van der Marel, *Phys. Rev. B* **81**, 125119 (2010).
- [50] G. Verbist, F. M. Peeters, and J. T. Devreese, *Ferroelectrics* **130**, 27 (1992).

- [51] G. A. Acket and J. Volger, *Phys. Lett.* **8**, 244 (1964).
- [52] G. A. Acket and J. Volger, *Physica* **32**, 1680 (1966).
- [53] G. Mattioli, F. Filippone, P. Alippi, and A. Amore Bonapasta, *Phys. Rev. B* **78**, 241201(R) (2008).
- [54] C. Lin, D. Shin, and A. A. Demkov, *J. Appl. Phys.* **117**, 225703 (2015).
- [55] R. Liu, L. Fang, Y. Hao, and Y. Chi, *Materials* **11**, 2156 (2018).
- [56] E. Finazzi, C. Di Valentin, and G. Pacchioni, *J. Phys. Chem. C* **113**, 3382 (2009).
- [57] G. Mattioli, P. Alippi, F. Filippone, R. Caminiti, and A. Amore Bonapasta, *J. Phys. Chem. C* **114**, 21694 (2010).